Elucidating Charge Transfer Processes and Enhancing Electrochemical Performance of Laser-Induced Graphene via Surface Engineering with Sustainable Hydrogel Membranes: An Electrochemist's Perspective

Mohsen Khodadadiyazdi[1,2,*], Aiswarya Manohar[1,2], Adrian Olejnik[2,3], Agata Smułka[4], Agnieszka Kramek[5], Mattia Pierpaoli[2,3], Mohammad Reza Saeb[6], Robert Bogdanowicz[2,3] and Jacek Ryl[1,2,*]

[1] Division of Electrochemistry and Surface Physical Chemistry, Faculty of Applied Physics and Mathematics, Gdańsk University of Technology, Narutowicza 11/12, 80-233 Gdańsk, Poland

[2] Advanced Materials Center, Gdańsk University of Technology, Narutowicza 11/12, 80-233 Gdańsk, Poland

[3] Department of Metrology and Optoelectronics, Gdańsk University of Technology, Narutowicza 11/12, 80-233 Gdańsk, Poland

[4] Department of Analytical Chemistry, University of Gdańsk, Wita Stwosza 63, 80-308 Gdańsk, Poland

[5] Faculty of Mechanics and Technology, Rzeszów University of Technology, Kwiatkowskiego 4, 37-450 Stalowa Wola, Poland

[6] Department of Pharmaceutical Chemistry, Medical University of Gdańsk, Hallera 107, 80-416 Gdańsk, Poland

*Corresponding authors: mohkhoda@pg.edu.pl (M.K), jacek.ryl@pg.edu.pl (J.R.)
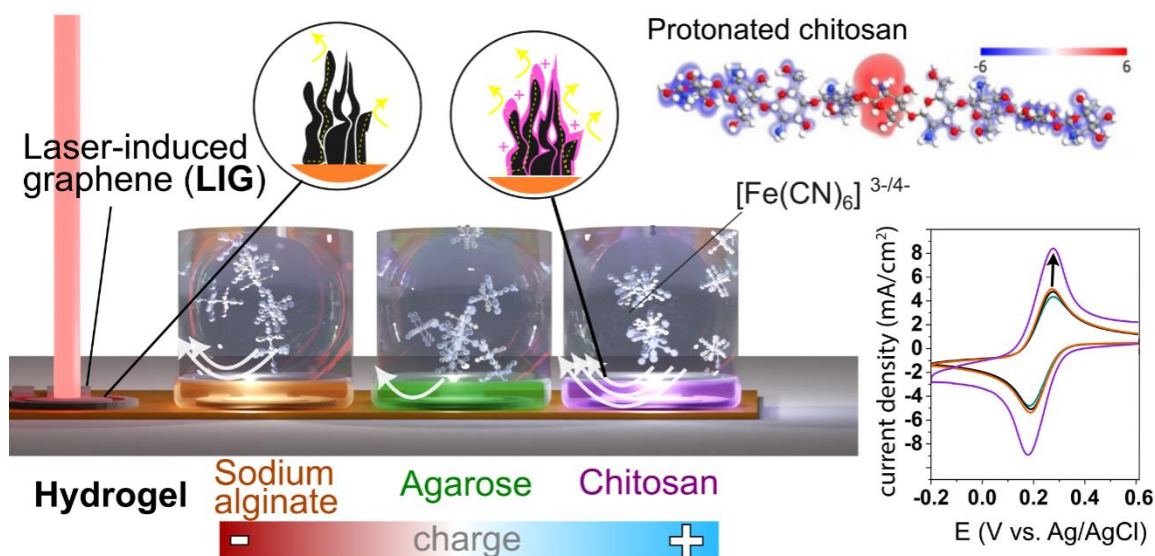
Abstract

Laser-induced graphene (LIG) has emerged as a promising solvent-free strategy for producing highly porous, 3D graphene structures, particularly for electrochemical applications. However, the unique character of LIG and hydrogel membrane (HM) coated LIG requires accounting for the specific conditions of its charge transfer process. This study investigates electron transfer kinetics and the electroactive surface area of LIG electrodes, finding efficient kinetics for the $[Fe(CN)_6]^{3-/4-}$ redox process, with a high rate constant of 4.12×10^{-3} cm/s and an electroactive area 28 times higher than the geometric area. The impact of polysaccharide HM coatings (cationic chitosan, neutral agarose and anionic sodium alginate) on LIG's charge transfer behavior is elucidated, considering factors like Ohmic drop across porous LIG and Coulombic interactions/permeability affecting diffusion coefficients, estimated from amperometry. Experimental findings are supported by ab-initio calculations showing a electrostatic potential map's negative charge distribution upon chitosan chain protonation, having an effect in over a two-fold redox current increase upon switching the pH from 7.48 to 1.73. This feature is absent for other studied HMs. It was also revealed that the chitosan's band gap was reduced to 3.07 eV upon acetylation, due to the introduction of a new LUMO state. This study summarizes the operating conditions enhanced by HM presence, impacting redox process kinetics and presenting unique challenges for prospective LIG/HM systems' electrochemical applications.

Keywords: Laser-induced graphene, hydrogel membrane, electrochemistry, electron transfer kinetics, diffusion coefficient

2

1. Introduction

Laser-induced graphene (LIG) with a 3D hierarchical, porous structure benefits from a fast production process, low-cost starting materials and a relatively green nature [1]. It can be considered as a rapid, pattering strategy, in which both production and patterning are carried out simultaneously, as compared to other graphene synthesis methodologies [2]. Its high electrical conductivity and high surface area have made LIG a promising electrode material for devices that harness chemical and electrochemical processes, such as electrocatalysts, energy storage and conversion, sensing and biosensing [3–5]. While the characteristic extended honeycomb lattice of graphene is absent throughout LIG structures, they usually possess numerous structural imperfections, such as pentagonal and heptagonal carbon rings and various functional groups, useful in the above-mentioned applications. LIGs can be post-processed through various strategies to enhance their functionality or induce new properties [6–8]. Their high surface area provides numerous sites for the (electro)deposition of nanoparticles, the grafting of various biomolecules and anchoring molecules, which are highly demanding for the detection of ionic species, small molecules and various biomarkers [9]. In addition, regardless of polyimide (PI) foils, LIG can be directly engraved onto biodegradable and biocompatible substrates, such as paper and chitosan (CS) that are in-line with sustainable and green materials criteria [10,11]. Lasing LIG with complex geometry on flexible substrates and the possibility to transfer it onto stretchable and adhesive hydrogels, conformal to natural skin, make it appealing for wearable bioelectronics, e-skin and soft robotics [12]. However, there are challenges associated with LIGs, such as significant dependence of the produced LIGs on lasing parameters, utilized raw materials, such as the brand of PI foil, or even the environmental stability of the LIGs during storage [4,13–15].

While bare LIG can be used as electrode materials for electrochemical applications, their integration with hydrogels can enhance their utility even further. Hydrogel coatings on LIG nanostructures can not only accommodate various biorecognition elements, such as enzymes, but they can also bridge the gap between LIG electrodes with electrons and/or holes as charge carriers and hydrated biological living tissues, for which ionic currents serve as charge carriers [16]. Moreover, HMs may have selective features, antifouling and/or antibacterial properties, desirable in (bio)sensing applications [17]. Hydrogel properties can be tailored to resemble the mechanical properties of living tissues, adhere to skin or even wet tissues *in vivo*, show

3

antibacterial and/or antifouling properties, and degrade on demand [18–20]. This has resulted in the wide application of hydrogel membranes (HMs), in modification of LIG-based electrodes [21]. For example, glucose oxidase (GOx) was incorporated into CS and utilized as a HM on Pt nanoparticles, decorated LIG electrodes for sweat glucose measurement [22]. Positively charged CS chains can immobilize negatively charged enzymes via electrostatic interactions, without adversely affecting their bioactivity.

However, these research studies don't consider the effect of HM itself, on the electrochemical performance of modified electrodes. HM can affect electrochemical behavior by affecting charge transfer kinetics and the mass transport rate in the vicinity of electrodes. For example, the decelerated mass transfer of analytes can result in a longer response time, for a biosensing device. The diffusion mass transfer of solutes through the porous hierarchical structure of hydrogels, that include free spaces at different length scales, i.e. from (sub)nano to microscale, is a complicated process [23], which can be affected by many factors, such as physical interactions between analytes and hydrophilic polymer chains, polymer chain conformational alternation, due to a local electric field in the vicinity of the electrode and electrostatic forces between HM and the analyte. It is not straightforward to measure the concentration gradient across hydrogel membranes covering LIG electrodes.

The porous and hydrated structure of hydrogels corresponds to the convection and diffusion mass transport of solutes through the hierarchical structure of hydrogels that include free spaces at different length scales, i.e. from (sub)nano to microscale [23]. Different theoretical models, such as the hydrodynamic theory, free volume and the obstruction theory have been developed to predict diffusivity in hydrogels, but with limited success [24–26]. The chemical structure of polymers constructing the HMs and the nature and density of crosslinking agents can significantly affect the diffusion and equilibrium adsorption of analytes.

HMs can not only affect the surface chemistry of the electrodes, but they can also affect the permeability of penetrants (e.g. redox species and analytes) [27]. Based on the size and chemistry of penetrants, which affect diffusivity and partitioning throughout the hydrogel, and the physicochemical properties of the hydrogel (e.g. porous structure, surface charge, hydration level and crosslinking density) the permeation of penetrants may change, affecting the electrochemical behavior of the electrochemical system. In other words, in the presence of an HM on the electrode surface, two phenomena may contribute: 1) charge transfer

4

kinetics, because of altered surface chemistry and, 2) permeability change, because of selective permeation throughout HMs. The system is more complex in the vicinity of electrodes, not only because of the concentration gradient and polymer chain-penetrant interactions, but also the external electric field are contributing mechanisms affecting the permeability of penetrants. However, electrochemical methodologies enable the prediction of an effective diffusion coefficient, without measuring the concentration gradient.

This work challenges the current state of the art, related to the description of charge transfer through interphase, composed of a highly porous LIG with limited electric conductivity and polysaccharide HMs, introducing varying mass transport effects for an electrochemically active, redox species. We provide an in-depth discussion of Ohmic drop consideration, across porous LIG, as well as the polysaccharide HMs' capability to alter LIG charge transfer, considering cationic (CS), neutral agarose (Agar) and anionic sodium alginate (Alg). Moreover, we reveal how and why LIG operating conditions affect redox process kinetics, emphasizing the importance of lasing optimization, partially limited by the HMs presence. Adequate consideration of electrode-dependent ohmic drop, frequency dispersion of capacitance, as well as the effect of electrostatic interactions, within the HM, on diffusion and the electrochemically active surface area (EASA) introduces new and important LIG characterization features.

2. Experimental methods

2.1. Reagents and materials

Commercial PI foils (thickness of 50μm) were purchased from DuPont (Kapton® HN). CS, Alg and Agar were purchased from Merck. Calcium chloride, acetic acid, glutaraldehyde (50%), phosphate-buffered saline (PBS) tablets and potassium hexacyanoferrate(II) trihydrate were purchased from Sigma.

2.2. LIG fabrication

LIG was fabricated using a commercial CO_2 laser cutting device (K40 model, from Shanghai ZX trading, power 40 W, wavelength 10.6 μm). In the first step, the geometry of LIG-based

5

electrodes was designed using an Inkscape software package. As shown schematically in **Fig. 1**, the electrodes include a circular working electrode (WE), 3 mm in diameter, which is encompassed by an incomplete ring, 0.5mm thick. The spacing between WE and CE was fixed at 0.5 mm. However, the utilization of LIG, as pseudo-RE, was not successful, as it cannot maintain a stable potential over time without further surface engineering. A CO_2 laser, in raster mode, was used to engrave patterns over PI sheets. Lasing was operated under ambient conditions. We used a laser speed from 100 to 200 mm/s and a laser power from 10 to 14%. The results from visual assessment are represented as a color matrix in the **SI file**, **Fig. S1**. For a laser power less than 10% (i.e. < 4 W) within tested speeds, LIG formation was incomplete on the PI foil for tested speeds. On the other hand, for high laser powers (>14%) or low laser speeds, LIG delamination or burnout formation was observable. No pretreatment was applied to PI sheets, before the lasing process.

2.3. Physicochemical properties measurement

The electrical resistance of LIGs was measured using a four-point probe equipped with a Keithley 2400, UK. Scanning electron microscopy (SEM) studies were performed using a Quanta 250 FEG microscope (ThermoFisher Scientific) equipped with a Schottky field emission gun, operating at an accelerating voltage of 30 kV after magnetron sputtering of a 5 nm gold layer. X-ray photoelectron spectroscopy (XPS) analyses were carried out using a K-Alpha spectrometer (ThermoFisher Scientific), operating an AlKα X-ray gun with a 250 μm spot diameter. The pass energy was set to 20 eV for the high-resolution spectra. The low-energy electron and Ar^+ ions flow was used for charge compensation with a final peak calibration and peak deconvolution using Avantage v5.9921 software, provided by the manufacturer. Raman measurements were performed using Xplora (HORIBA, France). The contact angle was measured with a DSA100 goniometer (Kruss, Germany), at room temperature, with 2 μL drops of water applied. The contact angle was recorded with a CCD camera and the average value of the wetting angle was determined using ADVANCE software, with the Young-Laplace method. Each measurement was repeated 20 times.

2.4. Electrochemical properties

6

Electrochemical studies were carried out on Biologic VSP-300 potentiostat/galvanostat. All measurements were done on 10 mM PBS solutions containing 5 mM of $K_3[Fe(CN)_6]$ and $K_4[Fe(CN)_6]$ as the redox probes. One PBS tablet was dissolved in 200 ml deionized water, according to the manufacturer's protocol, to obtain 10 mM PBS solutions. A three-electrode setup, with LIG as both the working electrode (WE, A = 0.085 cm^2) and the counter electrode (CE) and silver/silver chloride as reference electrode (RE), was used. All measurements were performed under ambient conditions (22°C).

Electrochemical impedance spectroscopy (EIS) measurements were done at open circuit potential (OCP) conditions, using perturbation peak-to-peak amplitude 10 mV and frequencies from 100 kHz to 100 mHz, 12 points per decade, after 5 min initial conditioning. Next, cyclic voltammetry (CV) measurements were carried out in the polarization range from -0.2 to 1.0 V, vs Ag|AgCl. Different scan rates, from 10 to 1000 mV/s, were employed.

Chronoamperometry (CA) tests were performed at applied voltages of +300 mV, +400 mV, and +500 mV, vs. Ag|AgCl for LIGs, and screen-printed carbon electrodes (SPCEs and DropSens 150, purchased from Metrohm), for reference. SPCEs were covered by 2.7 µL of CS or Alg solutions (0.2%) followed by drop-casting 2.7 µL of glutaraldehyde (3%) or a $CaCl_2$ (100 mM) solution, respectively. For making Agar coated SPCEs, 2.7 µL of Agar solution (0.2%) was drop cast on the SPCEs and left to dry under environmental conditions. For CA measurements, one droplet (100 µL) of 10 mM PBS solution containing 5 mM $Fe(CN)_6^{4-}$ redox probe was poured onto the SPCE or coated SPCEs and the experiments continued for 2 minutes.

2.5. Preparation of HM-coated LIG electrodes

Polysaccharide-based hydrogels were selected, as they are composed of natural biopolymers, which lies in-line with the sustainable materials criterion. Moreover, they are degradable and biocompatible polymers that can be tailored to make advanced functional materials [28]. Aqueous CS solutions at different concentrations were prepared by dissolving a predefined amount of CS in an aqueous solution of acetic acid (1 wt.%) by rigorous mixing for 5 h. For each concentration, 2 µL of the CS solution was dispensed over the WE and allowed to dry under ambient conditions. After that, 2 µL of the aqueous solution of glutaraldehyde (3 wt.%) was dispersed on the electrode surface for a few hours to crosslink chitosan. Before

7

electrochemical measurements, the electrodes were washed 3 times with deionized water to remove impurities. Alg was dissolved in deionized water by rigorous mixing for 5 h. The coating process was similar to CS, but 2 µL of 100 mM calcium chloride aqueous solution was used as a crosslinker. Divalent calcium ions enable ionic crosslinking for anionic Alg hydrogels. Agar was dissolved in hot water (90°C) under stirring to obtain a transparent solution. Then, 2 µL of this solution was dispersed over WE. No crosslinking agent is used for agarose, because this non-ionic PSA undergoes physical crosslinking via multiple hydrogen bonding interactions.

2.6. Molecular simulations

Molecular structures of CS oligo- or polymer were built in a Atomistic ToolKit Quantumwise (ATK, Synopsys, USA) environment [29]. These included monomer, 9-mer, 18-mer and 36-mer CS chains. The 9-mer chain served as the main model for the CS chain, for which both neutral and amine-protonated pyranose were considered (1/9 and 3/9 protonated groups). Pristine CS and its partially acetylated counterparts (1/9 and 2/9 acetylated mers) were also considered.

Density functional theory (DFT) calculations were performed using the Perdew–Burke–Ernzerhof (PBE) functional, within the generalized gradient approximation (GGA), as implemented in the package. The Linear Combination of Atomic Orbitals (LCAO) method, with norm-conserving pseudo-potentials, was applied [30,31]. The density of state spectra for CS monomers and chains was calculated using multi-pole boundary conditions (single k-point). Electron density maps and electrostatic potential maps were plotted using the default tool implemented in the ATK package.

Simulations of the ferrocyanide diffusion coefficient were performed using a DREIDING forcefield, with a charge equilibration scheme [32]. Three cells were employed: a 47 angstrom (Å) x 20 Å x 18 Å box filled only with water (density: 1 g/cm^3); a 47 Å x 20 Å x 18 Å box filled with water and 4 CS chains (density: 0.9 g/cm^3); a 50 Å x 40 Å x 40 Å filled with water and 4 CS chains (0.85 g/cm^3). Water filling was realized using Packmol, with the number of molecules, so that the perfect packing, with a 2 Å buffer layer, was achieved [33]. The first cell is a model of diffusion in water, the second in the "dense" CS (ca. 1 nm pores), and the third in the "sparse" CS (ca. 2 nm pores). CS molecules were placed in a straight conformation, parallel to

8

each other. Constant-temperature, constant-volume ensemble (NVT) dynamics were propagated for 100 ps in 300 K for each cell, with a single ferrocyanide molecule placed inside the channel. Diffusion coefficients are taken as slopes of the mean square displacement profiles, with respect to simulation time.

3. Results and discussion

3.1. The influence of lasing parameters on LIG electrochemistry

The properties of manufactured LIGs are highly sensitive to lasing parameters, where laser fluence is the most critical and should be in a proper range to obtain LIGs with efficient electrical conductivity and electrochemical activity [15,34–36]. **Fig. 1** reveals the influence of a 1% difference in laser fluence on physicochemical properties, LIG structure and electrochemical characteristics, while the full matrix for optimization of lasing parameters is presented and discussed in the **SI file**, **Fig. S1**.
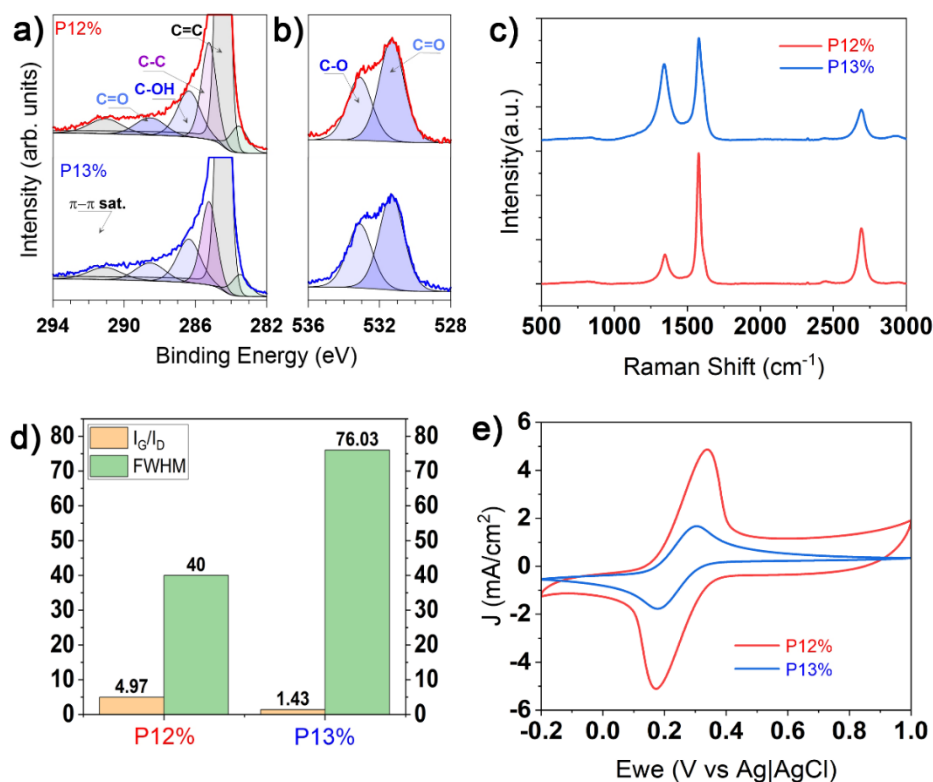

Fig. 1 – a,b) high-resolution *C 1s* and *O 1s* XPS spectra, respectively; c) Raman spectra with d) visualized I_D/I_G and FWHM; and c) CV scans (5 mM $Fe(CN)_6^{4-}$, scan rate ν = 50 mV/s), recorded for LIGs formed at various lasing powers (P12% and P13%) and with lasing speed 160 mm/s.

9

High-resolution XPS data is presented in **Fig. 1a** (C 1s) and **1b** (O 1s). The *C 1s* spectra reveal the complex carbon chemistry of both studied samples. The C=C bonds constitute a dominant contribution to the signal (BE at 284.2 eV [37]), originating from benzene rings in unprocessed Kapton® and the graphene structure in LIGs, the latter being very characteristic, due to its asymmetric shape and the appearance of a π-π* shake-up transition peak near 291.1 eV [38]. The remaining recorded *C 1s* peaks should be ascribed to carbon atoms single-bonded to oxygen or nitrogen (at 286.3 eV) and carbon atoms in the imide ring (at 288.6 eV) [39]. Notably, the peak at 283.4 eV is often recognized as C-C bonds in pentagonal Kapton® rings [40]. The last component (at 285.1 eV) should be ascribed to adventitious C-C/C-H species from atmospheric air exposure and, to some extent, C-N bonds. On the other hand, *O 1s* spectra were deconvoluted using two components, arising from the carbonyl group in the imide system (531.4 eV) and the ether group (533.1 eV), respectively [37,39].

Fig. 1c shows the Raman spectra for LIGs, which are produced under different operational conditions. For all samples, the D band is located at ~1345, the G band at ~1580 and 2D (or G') at ~2690 cm^{-1}. D (defect band) and G bands (graphitic band) correspond to structural defects and/or disorder, and sp^2 hybridized carbon atoms, respectively [41]. The full width at half maximum (FWHM) of the G band for LIGs produced at various powers, i.e. P12 and P13%, were estimated as 40 and 76, respectively, see **Fig 1d**. A much narrower peak for LIGs produced at 12% should be interpreted as a higher quality of graphene produced, with fewer defects, while a broader FWHM for P13% sample corresponds to the presence of defects, disorder and strain in the graphene structure [41]. In addition, the I_G/I_D ratio in the P12% sample is higher corresponding to the higher quality of graphene produced under these conditions [42]. The I_{2D}/I_G ratio for both samples is between 0.3-0.6, indicating that the created LIG contains multilayer graphene structures [43].

XPS analysis corroborates Raman spectroscopy data, allowing us to conclude the importance of lasing power on LIG surface chemistry. For the P12% sample, the graphitized carbon share is 2% higher than P13%. At the same time, the higher lasing power contributes to surface oxidation, as XPS reveals that the share of C-O and C=O moieties increases from approx. 26 at.% (when considering both *C 1s* and *O 1s* contributions) to 28.5 at.%. This is assisted by a slightly decreased share of C-C in pentagonal rings for the P13% sample, suggesting more

10

effective breaking of the imide bonds, often appearing under elevated heat [44]. XPS analysis for the Kapton® foil and peak deconvolution details are presented in the **SI file**, **Fig. S4** and **Table S1**, respectively**.**

The mechanism of PI conversion to LIG can be studied via the ReaxFF molecular dynamics methodology [45–47]. In this approach, all effects of the laser treatment are modeled via increased temperature (lasing power) and the dynamics are propagated for several nanoseconds. As a result, doped defected and twisted graphene layers are obtained, and various gases are liberated during this process. In the vacuum, the graphene sheet is typically terminated by H atoms, or the valences are unsaturated. When oxygen is present in the simulation box, the LIG yield is ca. 40% smaller and the product is oxygen-terminated, which is most presumably the cause of the amorphous graphene produced at higher laser powers.

Fig. 1c shows CV studies of the discussed LIG electrodes, tested with a $[Fe(CN)_6]^{3-/4-}$ redox probe, proving that current density and thereby the electrochemical activity of LIGs depends on laser parameters. Current density is the kinetic parameter describing the reaction rate. As the current density was only normalized by geometric surface area A, this parameter is primarily affected by the heterogeneous rate constant k and/or EASA, when using different LIG fabrication protocols. The first parameter is largely dependent on electrode chemistry and structure, while the latter may be enhanced by electrode geometry, both being subject to change for different lasing protocols. It is interesting to note, that P12% LIG is characterized by a more than two times higher peak current density compared to the P13% sample, which points out how much LIG laser power affects the charge transfer process. Yet, considering the XPS and Raman spectroscopy results, it appears that graphitic content is not the only factor determining electrochemical behavior. CV analyses were performed in a wide range of operating parameters: lasing power and laser speed, summarized in **SI file**, **Fig. S2**. These results reveal that 12% laser power and 160 mm/s laser speed appear to be the optimal conditions in our case, with the highest J and the lowest ΔE among the studied electrodes. The repeatability of LIG fabrication, in terms of CVs kinetics, was illustrated in **SI file**, **Fig. S3**.

For a reversible one-step, one-electron electrochemical reaction, the anodic-to-cathodic CV peak split, ΔE, should be approximately 59 mV at any scan rate, a value unmet for either of the studied LIG samples [48]. Aside from the irreversibility of the charge transfer process, disordered electrochemical behavior, such as enhanced peak separation in CV curves, may be

11

an effect of an Ohmic drop. Ohmic drop is usually related to the low ionic conductivity of the electrolyte and corresponds to high electric resistance between WE and RE. Yet, considering the relatively high electric resistivity of conductive carbon species and the low cross-sectional surface area of porous LIG structures, high electric resistance between WE and CE may also lead to an Ohmic drop. The asymmetric shape of the CV curve, visible in **Fig. 1c**, confirms the presence of such an Ohmic drop. Similar cases may be observed for conductive 3D-printed composites [49].

SEM micrographs reveal LIG surface morphology and its variation under different lasing conditions, see **Fig. 2a** and **2b**, testifying to the formation of highly porous structures with a developed surface area for all investigated LIG samples. An ImageJ software package was used to analyze SEM images. The P12% sample shows distinct circular pores, with diameters ranging from 3 to around 20 μm. These pores are the passageways for hot released gases that are produced as by-products during the lasing process of PI foils [50]. The pore size for the P13% sample is similar, yet much less ordered, with high magnification images revealing some kind of powdered features, dissimilar to graphene nanostructures. Their presence may be responsible for decreased electrical conductivity and, supposedly, diminished electrochemical activity of the P13% samples.

As lasing power increases, the total production yield of LIG plummets, because of higher mass loss from the system. Under these conditions, smaller LIG clusters are formed. The burst and violent release of hot gases can probably detach and carry small LIG-like residues from underlying structures. However, the speed and temperature of gaseous by-products drop significantly at the exit point, resulting in the precipitation of these materials on the LIG surface, which is probably the source of the fractal-like structures observed in **Fig. 2c.** At an even higher laser power, the spread of graphene-like debris around the LIG electrodes, was observable under an optical microscope. In addition, results from ReaxFF simulations indicate that the release of by-product gases will result in high porosity structures, as observable in **Fig. 2**.
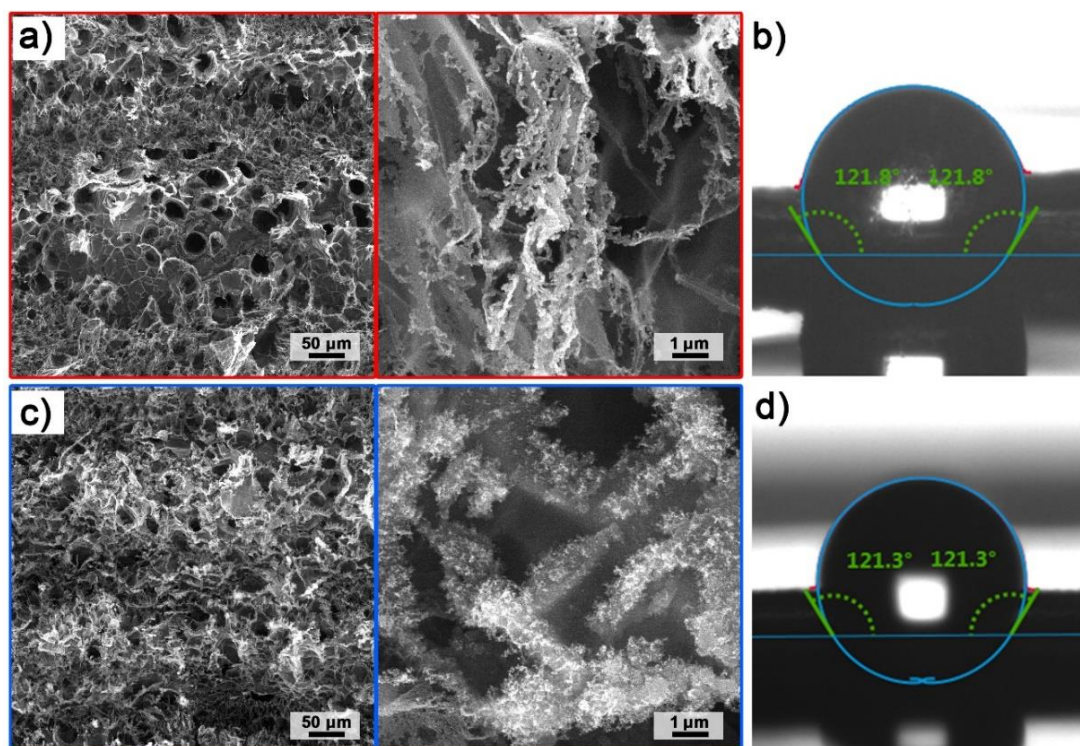
Fig. 2 – Surface properties: a,c) SEM topography images and b,d) contact angle analysis of LIG samples prepared at different lasing powers: a,b) P12%; c,d) P13%

Contact angle measurements, allowing the assessment of LIGs hydrophilicity, are given in **Fig. 2b** and **2d**, for P12% and P13% samples, respectively. The resulting values of the water contact angles indicate their hydrophobic nature, with CA exceeding 120° regardless of lasing parameters, which corresponds to a low share of polar moieties by XPS analysis, only slightly higher for the P13% sample. LIG porous (at lower length scales) and grooved (at higher length scales) geometry, as determined by SEM results, may further contribute to hydrophobicity, through the Cassie-Baxter state [51]. The low wettability offered by as-fabricated LIGs may result in sub-optimal electrochemical behavior, without post-processing surface engineering, diminishing effective EASA values.

3.2. Consideration of the sub-optimal LIG electric conductivity in voltammetry studies

In the majority of electrochemical experiments, the ohmic drop appears between WE and RE, due to the low ionic conductivity of the electrolyte [52]. Various strategies, such as current interrupt (CI), EIS and potential step can be used to compensate for ohmic drop. Some of these

13

strategies are embedded in software that comes with potentiostat and are based on hardware compensation [53]. Graphene has high and low electrical conductivity parallel and perpendicular to planes of hexagonal rings, respectively [54]. Moreover, defects in the extended hexagonal structure of graphene, pendant functional groups and nanoplatelet stacking can diminish electrical conductivity. The porous structure of LIG results in a lower cross-section, reducing electrical conductivity. The electric resistance measured by the four-probe technique, for LIGs at different laser parameters, revealed sheet resistance to be as low as around 1.9±0.1 Ω/sq for P12% while reaching 2.5±0.2 Ω/sq (more details in the **SI file**, **Table S2**) for P13%, comparable to other reports [34].

For the analyzed LIG samples, one must consider a different source of the ohmic drop between the WE and the CE electrodes, forcing an alternative approach, which may be performed based on manual correction after the measurements. **Fig. 3** compares the raw exemplar result with its compensated versions for the P12% sample. One methodology that can be applied for manual compensation of the ohmic drop is to assume that the potential "felt" by the working electrode V(t) is equal to its true potential E(t) minus the IR voltage drop, according to the equation (1) [52]:

$$V(t) = E(t) - R \times I(t) \tag{1}$$

where R is the resistance in series connection to the Randles circuit, then, the true potential is obtained by subtraction and the total current is plotted against the true potential. After such a correction, peak separations are expected to decrease, because higher currents correspond to a higher ohmic drop, which eventually results in decreased peak splitting, as shown with a red curve in **Fig. 3**, for different values of series resistance. However, after such compensation, the shape of the CV does not change, in contrast to hardware correction.
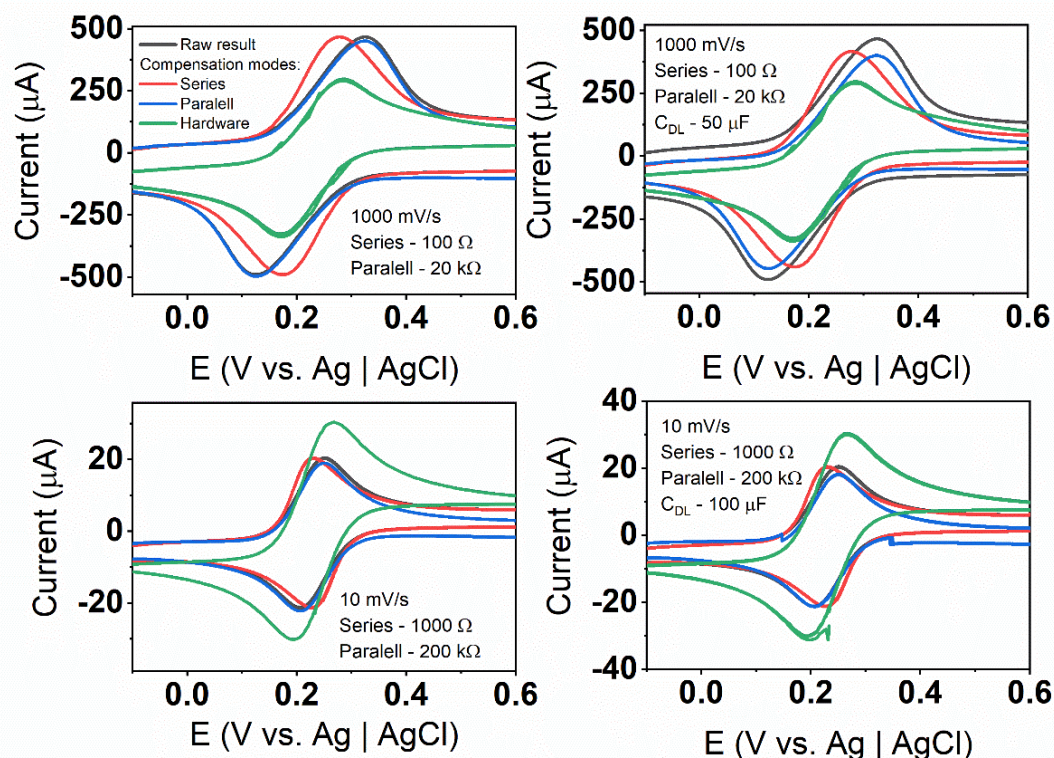
Fig. 3 – Effect of the hardware and manual ohmic drop corrections for sample P12%.

An alternative approach for ohmic compensation is to assume that there is a parasitic process occurring in parallel to electrochemical charge transfer and double-layer charging. Thus, the total current measured by the potentiostat would be equal to (2):

$$I_{Total} = I_{Electrochemical} + \frac{U}{R} \tag{2}$$

where R is the resistance of the hypothetical parallel process. Smaller resistance results in a greater parasitic current. Such a process is equivalent to the additional resistance parallel to the Randles circuit. The electrochemical currents of interest can be obtained by the subtraction of the parasitic current (effectively subtracting a straight line from the CV curve). This kind of correction is expected to cause only a minor peak separation reduction, because subtraction is a linear function of potential, but it has a better alignment with the zero-current line. This effect can be observed as a blue curve in **Fig. 3**, where the current from a parallel resistor with different resistance was subtracted. In both manual corrections, the influence of double-layer capacitance was also artificially subtracted (a 50 µF capacitor). No combination of resistors and capacitors in the manual corrections was able to reproduce the hardware

15

correction of the potentiostat. This issue is even more important, as in the case of low scan rates, hardware correction yields larger peak separation compared to the raw data – which is not intended. Manual corrections, on the other hand, behave similarly regardless of the scan rates and regardless of whether the double-layer effects are subtracted or not.

3.3. Surface engineering of LIGs by polysaccharide HM-coating

HM coatings can affect the kinetics of redox processes by impacting the mass transfer of redox species, altering the surface chemistry and wettability of the electrode. In addition, the equilibrium concentration of redox species within hydrogel membranes, covering electrodes, may differ from the bulk electrolyte. Here, we have selected different polysaccharide hydrogels to tailor the ionic transport within the diffusion layer and determine their influence on the kinetics of the redox processes, choosing representatives of cationic (CS), anionic (Alg) and non-ionic (Agar) polysaccharides, visualized in **Fig. 4a**. These biocompatible and biodegradable polymers can be utilized in 3D printing, which facilitates their usage in rapid manufacturing techniques [51].

The introduction of HM coatings on the LIG surface affects the properties of the material in different ways, see **Fig. 4b**. The Agar and CS-coated surfaces become super hydrophilic, as a result of the modification. For CS, a rapid soaking of the water droplet into the electrode structure makes it difficult to precisely measure the contact angle, as seen in **Fig. 4c**. This effect is possible, due to the presence of positively charged $-NH_3^+$ groups with hydrogen bonding capability, fostering strong interactions with water molecules through both electrostatic and hydrogen bonding interactions. Agar HM, with its $-OH$ groups facilitating hydrogen bonding with water, exhibited moderate enhancement of LIG hydrophilicity, providing some affinity for water molecules without the pronounced electrostatic interactions observed with CS. In contrast, Alg-covered LIG had a contact angle decreased by $36°$ vs an unmodified surface, yet the effect is incomparable to other HMs. Lacking a strong hydrogen bonding capability and featuring a net negative charge displayed a lesser effect on LIG electrode hydrophilicity compared to chitosan. The above observations are confirmed by the XPS data, located in the **SI file**, **Fig. S5**, while SEM images in the **SI file**, **Fig. S6** visualize a thin layer of CS in a dried state over the LIG structure.

From the electrochemical behavior perspective, substantially improved electrode wetting should affect EASA increase, and, as a consequence, current densities of the studied redox process. The CV recorded for HM-coated LIG electrodes are presented in **Fig. 4d** and **Fig. 4f**, for the P12% and P13% samples, respectively. Both of these figures indicate that while anionic Alg and non-ionic Agar do not show a significant effect on electrochemical behavior in this redox system, when compared to bare LIG electrodes, cationic CS coatings enhanced the peak current densities significantly.
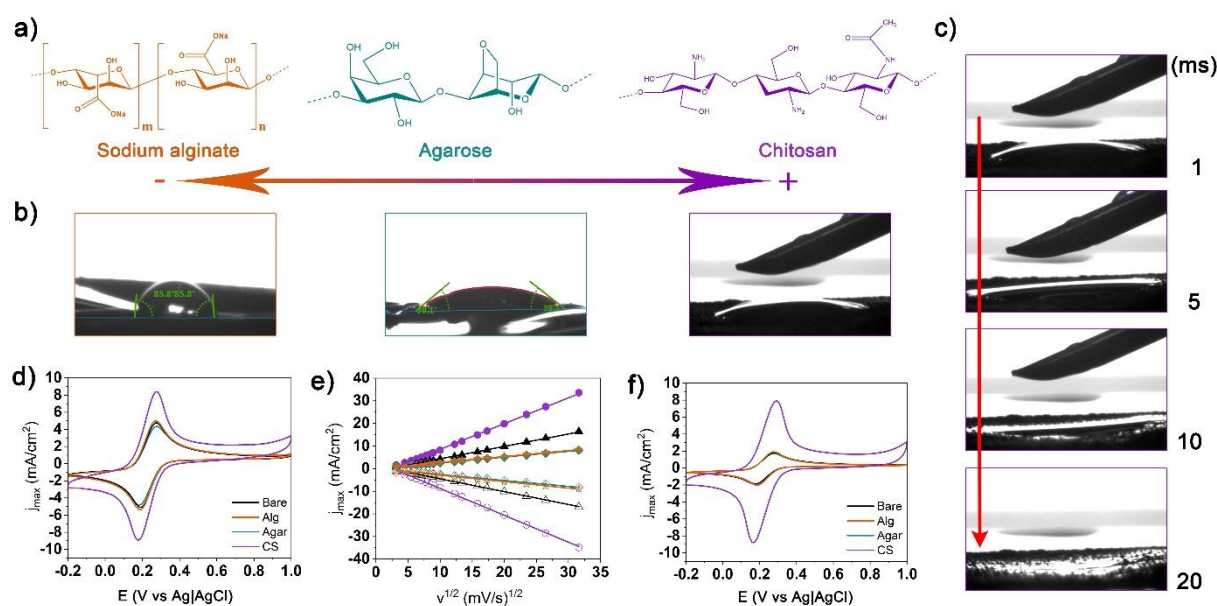

Fig. 4 – a) chemical structure of studied polysaccharide HMs and b) contact angle measured for P12% with different HMs (CS, Agar, Alg); c) water droplet soaking rate into CS HM at P12% sample; d,f) CVs for HM-coated P12% and P13% LIG samples, respectively (5 mM Fe(CN)$_6$$^{4-}$, v = 50 mV/s); e) RS plot for bare and HM-coated LIGs.

Interestingly, bare P13% samples show hampered redox kinetics when compared to P12%, yet the CS-coated P13% behaves similarly to the CS-coated P12%. This is an interesting phenomenon, which might indicate that the CS-coating has some ability to negate the sub-optimal LIG processing conditions, leading to altered topography and surface electrostatic interactions. Because of HM's porous structure and chemistry, the effective diffusion of solutes could be different. In addition, coulombic interactions between the hydrogel and redox species correspond to different partitioning for various HMs with different charges. The collective effect of these phenomena results in different permeability and altered electrochemical responses.

To better understand the influence of different HMs on D value we have applied chronoamperometry (CA) tests, first focusing on CS coatings, as their electric affinity allows for a superior increase in electron transfer kinetics, see **Fig. 5**. These experiments were first performed on flat screen-printed carbon electrodes (SPCEs) and hydrogel-coated SPCEs. It was assumed that for flat SPCE, the EASA is equal to its geometric surface area. The theoretical background and the obtained results are presented in the **SI file**, **section S5,** where Cottrell's and Berzins–Delahay equations were utilized to estimate the diffusion of $Fe(CN)_6^{3-/4-}$ through the CS HM, as eq. (3) [55].

$$I_{total}(t) = nFACk \times exp\left(\frac{k^2}{D}t\right) \times erfc\left(\frac{k}{\sqrt{D}}t\right) + I_c \times exp\left(\frac{-t}{\tau}\right) + I_s \qquad (3)$$

where n is the number of electrons transferred (equal to 1), F is the Faraday constant equal to 96500 C/mol, A is EASA, C is a concentration in the bulk electrolyte, I_c is a pre-factor related to the capacitive current, I_s is a steady-state residual current and τ is an RC circuit time constant of the system related to the discharge of the double layer.
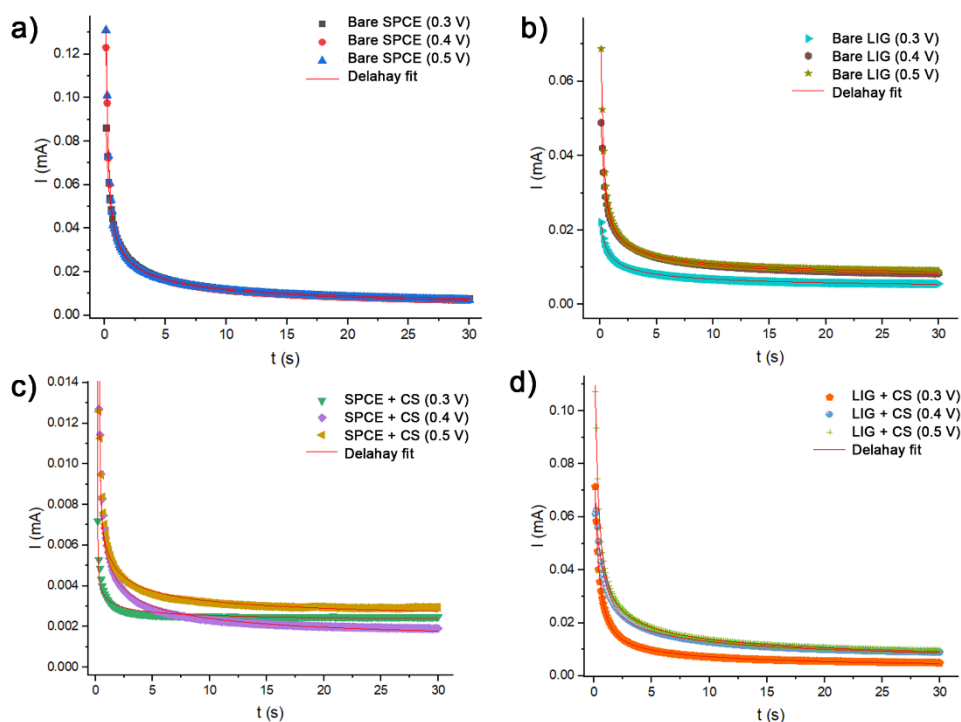

Figure 5 – CA results with the Berzins–Delahay function fitting for: a) bare SPCE; b) CS-coated SPCE; c) bare LIG; d) CS-coated LIG.

The applied strategy was validated using the obtained diffusion coefficient of the redox probe in a 0.1 M KCl solution and reported results in the literature [56,57] as discussed in the **SI file**, **section S5**. Based on the Delahay equation, the D in the PBS solution was estimated to be 1.09×10^{-6}, which is approximately one-fifth that of the value in 0.1 M KCl, corresponding to a higher solvation state. The diffusion coefficients for the redox probes depend significantly on the utilized electrolyte and its concentration, which highlights the reason for the difference between our results.

According to the methodology described in the **SI file**, **section S5.1**, a series of k and D values was estimated for SPCE, as represented in **Table 1**. According to the obtained results, the modified Berzins–Delahay equation describes the system well, as reflected in the fitted parameters, i.e. the R^2, the chi^2 values and the negligible standard errors of each calculated quantity (see **SI file**, **section S5.2**). For simplicity, it was assumed that the D of the reduced and oxidized forms of the redox probes are equal.

Table 1 – Estimated values for D and k, for bare and HM-coated SPCE (CS, Alg, Agar).

	Bare SPCE	Alg-coated SPCE	Agar-coated SPCE	CS-coated SPCE
D x10^{-6} [cm^2/s]	6.98	3.99	2.40	0.38
k x10^{-3} [cm/s]	4.80	3.56	3.20	0.49

The CS-coated SPCE exhibits lower D for $[Fe(CN)_6]^{3-/4-}$ compared to the bare SPCE, indicating that redox species diffuse into the hydrogel at lower rates compared to the PBS solution. This can be correlated to the electrostatic attraction between positively charged CS chains and $[Fe(CN)_6]^{3-/4-}$ species that retard their acceleration in the electric field. Part of negatively charged $[Fe(CN)_6]^{3-/4-}$ species, which diffuse through free volumes between positively charged polymeric chains are attracted by local electric fields around NH_3^+ moieties on CS chains that oppose the electric field of electrode, decreasing the speed of the redox probes. However, the improved equilibrium absorption of negatively charged redox species likely led to enhanced partitioning and heightened permeability across the hydrogel membrane [58]. The diffusivity and partitioning of penetrants tend to have opposing effects that counteract each other. Consequently, the lowest diffusion coefficient can be expected for the positively charged chitosan, while the highest diffusion coefficient is anticipated for the negatively charged Alg,

19

due to the inverse relationship with partitioning, which is influenced by surface charges. For the non-ionic Agar, an average diffusivity can be expected.

The D values, estimated in the HM environment and using SPCEs, were used to estimate k and EASA values for HM-coated LIGs, as depicted in **Table 2**. Bare LIG and SPCE exhibit similar heterogeneous transfer rates, yet regardless of their hydrophobic nature, LIG possesses higher EASA, influencing superior charge transfer kinetics. Supplementary EIS measurements in the **SI file**, **Fig. S7** confirmed that the charge transfer resistance is 72.46 and 11.22 Ω for SPCE and LIG (P12%), respectively. LIG has an anionic surface charge, because of oxygenated carbonyl or hydroxyl functional groups (see **Fig. 1a**). Accordingly, positively charged CS chains can adsorb at graphene platelets, while negatively charged Alg adsorption is hard. However, regardless of molecular adsorption, the mechanical interlocking of hydrogels, inside the porous LIG structure, helps their fixation onto the electrode. Accordingly, one can expect the best molecular contact between CS polymer chains and graphene, and the worst for Alg. This indicates the highest available electrochemically active surface area (EASA) for ferricyanide redox probes in the CS matrix and the lowest for Alg.

The EASA for discussed LIG samples, including the effect of HM surface engineering was estimated using the Randles–Sevcik (RS) equation, eq. (4), for a one-electron, one-step process [52].

$$i_{(a,p)} = 2{,}99 \cdot 10^5 \alpha^{(1/2)} ACD^{(1/2)} v^{(1/2)} \tag{4}$$

where v is the CV scan rate, α is the symmetry factor (established as 0.5) and D values were taken from **Table 1**. The RS plot for bare and CS-coated LIGs is depicted in **Fig. 5e**.

Table 2 – Estimated k and EASA values for bare and HM-coated LIG P12% sample.

	Bare LIG	Alg-coated LIG	Agar-coated LIG	CS-coated LIG
k x10^{-3} [cm/s]	4.12	7.99	6.78	3.88
EASA$_{(a)}$ [cm^2]	0.25	0.16	0.20	2.34
EASA$_{(c)}$ [cm^2]	0.26	0.17	0.20	2.33

Electrode kinetics studies allow us to draw important conclusions regarding the studied processes. The EASA of LIG is x3 larger than its geometric surface area of 0.085 cm^2. Surface

engineering by Agar or Alg does not translate for enhanced EASA, while hampering the diffusion rate. On the other hand, CS HM is capable of boosting the EASA by an additional order of magnitude, with a total of x28 EASA increase, allowing it to take full advantage of the hierarchical porous LIG structure. CS crosslinking optimization may have an additional effect on redox kinetics, as discussed in the **SI file**, **Fig. S8**.

The effect of pH on the charge transfer kinetics through the HM-coated LIG electrode/electrolyte interface is illustrated in **Fig. 6**. These studies were carried out for P12% LIG samples and the pH was adjusted by 1M HCl or 1M NaOH solutions. ZIR compensation was applied for all samples. We observed a significant change in pH 1.95 and pH 3.07 indicating the effect of high acidity conditions on CV plots.
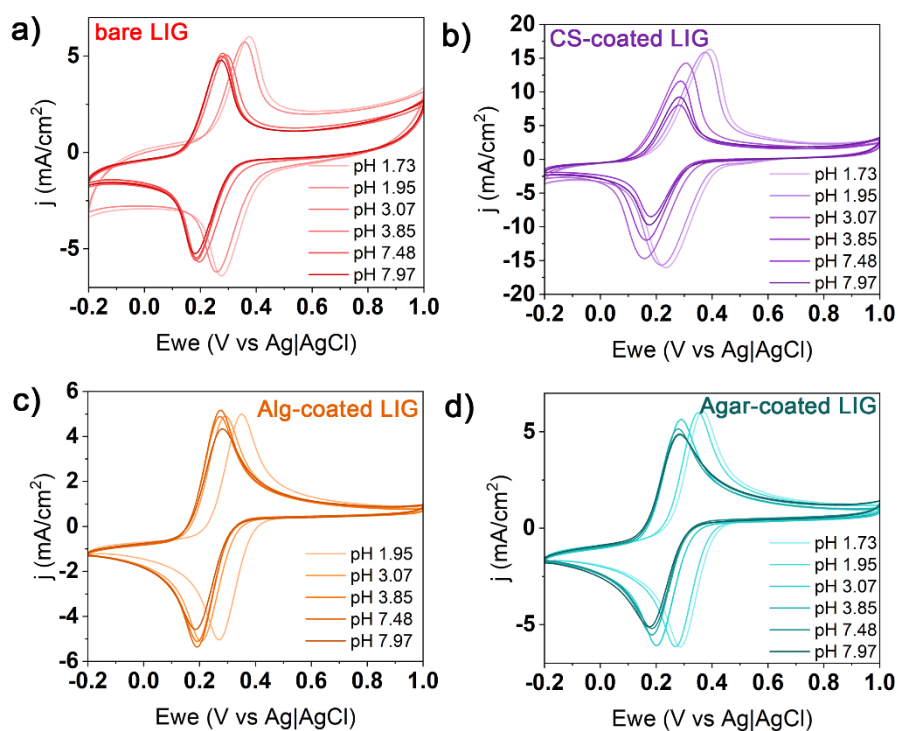

Fig. 6 – CVs for a) LIG and b-d) HM-coated P12% LIG samples: b) CS; c) Alg; d) Agar, recorded at different electrolyte pH (5mM $Fe(CN)_6^{4-}$, ν = 50 mV/s).

As shown in this plot, the pH has a two-fold effect, shifting the peak potential into a slightly positive potential range with the increase of electrolyte acidity and affecting $Fe(CN)_6^{4-/3-}$ redox kinetics. For bare LIG electrodes (**Fig. 6a**), a non-faradaic current increase is observable for acidic pH, which may suggest gradual graphene decomposition by electrolyte [59]. Among the

studied polysaccharide HMs the dominant effect of pH on the CS coating (**Fig. 6b**) persists in a wide range of tested pH.

The electrostatic potential (ESP) maps of a single CS 9-mer chains in neutral and two protonated states are illustrated in **Fig. 7**, to support the pH effect on the charge transfer kinetics through the CS-coated, LIG P12% sample.
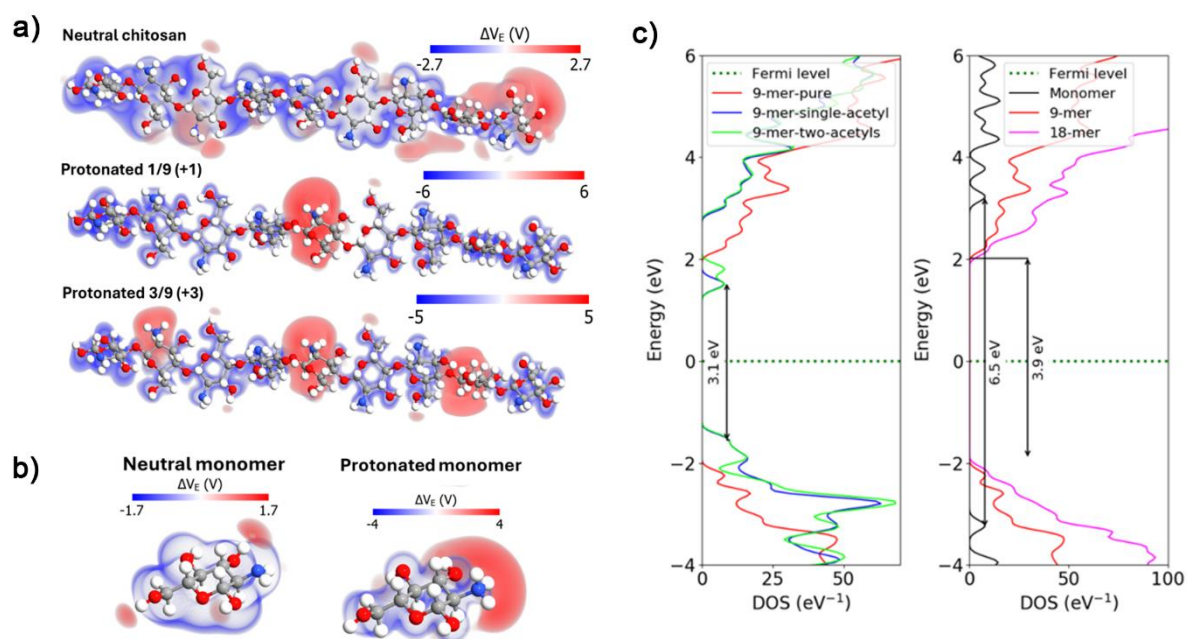

Fig. 7 – Molecular *ab-initio* simulations of CS oligo- or polymer structures: a, b) Electrostatic potential mapping (ESP) of the CS chains in different protonation states and CS monomers; the bar shows the regions of high (red) and low electron density (blue), c) The density of states (DOS) of acetylated 9-mers (left) and pristine 9- and 18-mer version along with monomer (right). The band gap values were marked in the graphs.

A neutral CS molecule is negatively charged in most regions with some positive charge accumulated on the –OH protons, with the same tendency also observed for monomers, both seen in **Figs 7a** and **7b**. In the case of polymeric chains, an additional positive charge is also present on the terminal mer, rendering local –OH groups more acidic. However, when the protonated CS is regarded, a significant positive charge is concentrated at every –NH₃⁺ group [60,61]. The density of states (DOS) map of the monomer (**Fig. 7c**) shows a 6.39 eV HOMO-LUMO gap with the Fermi level in the middle of the gap. For the polymer, the gap is equal to

4.55 eV in the 9-mer and 18-mer versions. Thus, CS reveals an insulating character. However, when the chain contains acetylated mers (with an amide group), an additional DOS band appears above the Fermi level and becomes the LUMO. This shift, effectively narrows the bandgap to 3.07 eV, regardless of the number of acetyl groups in the chain (one or two groups yield the same position on the energy scale).

The CV peak in the current registered for pH 1.73 is over two times higher, compared to pH 7.48 and 7.97 (**Fig. 6b**), the effect is not as prominent in less acidic media. This effect should be correlated with inducing more positive charges, i.e. the formation of more $-NH_3^+$ species, on the CS chains at higher protonation states, as was predicted from electrostatic potential maps in **Fig. 7**. Repulsive forces between positively charged polymeric chains can result in a more accessible free volume for redox species to diffuse into, thereby increasing the D values (for CS HM increase from 3.8×10^{-7} in pH 7.48 to 2.38×10^{-6} for pH 1.95).

The HM coating constitutes, to some extent, an effective surface engineering technique in a neutral environment, as it allows maintenance of a stable redox peak potential under pH fluctuations. HM presence limits hydronium ions' activity at the reaction plane. Discussing the pH effect, one must consider that the hydrogel layer thickness surpasses the diffusion layer thickness, thus leading to an assumption that the bulk electrolyte pH and concentration may not reflect the conditions within the hydrogel layer.

Conclusions and perspectives

This study investigated charge transfer processes and electrochemical performance of laser-induced graphene (LIG) through surface engineering with sustainable hydrogel membranes (HMs), like sodium alginate (Alg), agarose (Agar) and chitosan (CS), from an electrochemist's perspective. Key findings and phenomena include:

✓ Ohmic drop correction is crucial for accurate analysis of LIG electrodes, which can be done manually or by considering parallel parasitic processes occurring at the electrode-electrolyte interface.

23

- ✓ Coulombic interactions between hydrogels and redox species, like $[Fe(CN)_6]^{3-/4-}$ affected partitioning, permeability and electrochemical responses through attractive/repulsive forces.

- ✓ Cationic CS coatings significantly enhanced redox peak current densities compared to bare LIG, while anionic Alg and non-ionic Agar showed minimal effects, possibly due to electrostatic interactions.

- ✓ CS coating lowered diffusion coefficients (D) of $[Fe(CN)_6]^{3-/4-}$ redox species, due to electrostatic attraction, retarding acceleration in the electric field caused by the applied potential.

- ✓ LIG electrodes exhibited ~2 times faster heterogeneous transfer rates compared to screen-printed carbon electrodes (SPCEs), possibly due to the higher conductivity and surface area of LIG.

- ✓ At pH 1.73, higher protonation of CS increased peak currents over 2 times compared to pH 7.48 and 7.97, due to repulsive forces between positively charged polymer chains creating a more accessible porous structure.

- ✓ CS coatings dramatically increased electroactive surface area (EASA) and the concentration of Fe redox probes inside the hydrogel, boosting charge transfer kinetics through attractive electrostatic interactions.

From an electrochemist's perspective, the tunable 3D morphology of laser-induced graphene (LIG) offers flexibility in electrochemical applications by tailoring the structure by adjusting laser parameters, environment, substrate and composition to control properties, like surface area, porosity and defects. However, widespread practical adoption of LIG electrodes faces challenges related to the cost of raw materials, energy consumption, fabrication time, number of steps, post-treatments, marketability, scale of production and profitability.

Incorporating other nanomaterials, like nanowires, nanospheres, nanowalls and nanocubes on the LIG surface, can improve LIG's inherently low conductivity and electrocatalytic response. While wetting properties influence the electrode-electrolyte interface, the synergistic effect of wetting and doping LIG is poorly understood, from an electroanalytical perspective. Current composites, with non-uniform doping, limit the diversity of electrochemical probes that can be effectively incorporated.

24

From an electrochemist's view, efforts are needed to improve the porous LIG structure's robustness and durability, which can lead to electrode fouling and surface changes over time, without compromising cost considerations that make LIG attractive. LIG's high surface area offers benefits, like improved electrochemical performance, while scalable fabrication and automation enable potential cost reductions.

Electrochemical research focuses on optimizing LIG synthesis, developing LIG into reliable sensors by understanding phenomena, like charge transfer and mass transport, and exploring functionalization strategies. Batch-to-batch consistency of LIG electrodes remains a challenge compared to commercial screen-printed electrodes. Crucially, the proposed LIG electrochemical sensors often lack *in vivo* or on-site real-world testing data, limiting understanding of their true feasibility, long-term stability/durability and susceptibility to interferents/fouling from complex sample matrices, like biological fluids.

While advantages like low cost, upcycling, biodegradability and flexibility make LIG promising for sustainable electrochemical sensing and devices, an electrochemist's perspective emphasizes addressing limitations in scalability, uniformity, durability, real-world reliability and the fundamental understanding of physicochemical processes for LIG to achieve widespread practical electroanalytical adoption.

Acknowledgements

CRediT author statement

Conceptualization: M.K. and J.R.; Methodology: M.K., A.M., A.O. and J.R., Validation: M.K. and A.M., Formal analysis: A.M., A.O.; Investigation: M.K., A.M., A.O., A.S. and A.K.; Resources: R.B. and J.R.; Data Curation: M.K. and A.M.; Writing – Original Draft: M.K., A.M., A.O., M.P., R.B.

25

and J.R.; Writing – Review & Editing: M.R.S., R.B. and J.R.; Visualization: A.M., A.O. and M.P.; Supervision – J.R.; Project administration – M.K. and J.R.; Funding acquisition: M.K., M.P. and R.B.

References

[1] R. Ye, D.K. James, J.M. Tour, Laser-Induced Graphene: From Discovery to Translation, Advanced Materials 31 (2019) 1803621. https://doi.org/10.1002/adma.201803621.

[2] W. Gao, The Chemistry of Graphene Oxide, in: W. Gao (Ed.), Graphene Oxide, Springer International Publishing, Cham, 2015: pp. 61–95. https://doi.org/10.1007/978-3-319-15500-5_3.

[3] Y. Ben-Shimon, C.P. Sharma, C.J. Arnusch, A. Ya'akobovitz, Freestanding Laser-Induced Graphene Ultrasensitive Resonative Viral Sensors, ACS Appl. Mater. Interfaces 14 (2022) 44713–44723. https://doi.org/10.1021/acsami.2c08302.

[4] A.C. Bressi, A. Dallinger, Y. Steksova, F. Greco, Bioderived Laser-Induced Graphene for Sensors and Supercapacitors, ACS Appl. Mater. Interfaces 15 (2023) 35788–35814. https://doi.org/10.1021/acsami.3c07687.

[5] R. Correia, J. Deuermeier, M.R. Correia, J. Vaz Pinto, J. Coelho, E. Fortunato, R. Martins, Biocompatible Parylene-C Laser-Induced Graphene Electrodes for Microsupercapacitor Applications, ACS Appl. Mater. Interfaces 14 (2022) 46427–46438. https://doi.org/10.1021/acsami.2c09667.

[6] A. Chhetry, Md. Sharifuzzaman, H. Yoon, S. Sharma, X. Xuan, J.Y. Park, MoS$_2$-Decorated Laser-Induced Graphene for a Highly Sensitive, Hysteresis-free, and Reliable Piezoresistive Strain Sensor, ACS Appl. Mater. Interfaces 11 (2019) 22531–22542. https://doi.org/10.1021/acsami.9b04915.

[7] N.T. Garland, J. Schmieder, Z.T. Johnson, R.G. Hjort, B. Chen, C. Andersen, D. Sanborn, G. Kjeldgaard, C.C. Pola, J. Li, C. Gomes, E.A. Smith, H. Angus, J. Meyer, J.C. Claussen, Wearable Flexible Perspiration Biosensors Using Laser-Induced Graphene and Polymeric Tape Microfluidics, ACS Appl. Mater. Interfaces 15 (2023) 38201–38213. https://doi.org/10.1021/acsami.3c04665.

[8] J. Zhu, M. Cho, Y. Li, I. Cho, J.-H. Suh, D.D. Orbe, Y. Jeong, T.-L. Ren, I. Park, Biomimetic Turbinate-like Artificial Nose for Hydrogen Detection Based on 3D Porous Laser-Induced Graphene, ACS Appl. Mater. Interfaces 11 (2019) 24386–24394. https://doi.org/10.1021/acsami.9b04495.

[9] Z. Wan, N.-T. Nguyen, Y. Gao, Q. Li, Laser induced graphene for biosensors, Sustainable Materials and Technologies 25 (2020) e00205. https://doi.org/10.1016/j.susmat.2020.e00205.

[10] B. Kulyk, B.F.R. Silva, A.F. Carvalho, S. Silvestre, A.J.S. Fernandes, R. Martins, E. Fortunato, F.M. Costa, Laser-Induced Graphene from Paper for Mechanical Sensing, ACS Appl. Mater. Interfaces 13 (2021) 10210–10221. https://doi.org/10.1021/acsami.0c20270.

[11] H. Hamidi, J. Levieux, C. Larrigy, A. Russo, E. Vaughan, R. Murray, A.J. Quinn, D. Iacopino, Laser induced graphene (LIG) biosensors derived from chitosan: Towards sustainable and green electronics, Biosensors and Bioelectronics: X 15 (2023) 100403. https://doi.org/10.1016/j.biosx.2023.100403.

[12] Y. Lu, G. Yang, S. Wang, Y. Zhang, Y. Jian, L. He, T. Yu, H. Luo, D. Kong, Y. Xianyu, B. Liang, T. Liu, X. Ouyang, J. Yu, X. Hu, H. Yang, Z. Gu, W. Huang, K. Xu, Stretchable graphene–hydrogel interfaces for wearable and implantable bioelectronics, Nat Electron 7 (2023) 51–65. https://doi.org/10.1038/s41928-023-01091-y.

[13] M. Abdulhafez, G.N. Tomaraei, M. Bedewy, Fluence-Dependent Morphological Transitions in Laser-Induced Graphene Electrodes on Polyimide Substrates for Flexible Devices, ACS Appl. Nano Mater. 4 (2021) 2973–2986. https://doi.org/10.1021/acsanm.1c00101.

[14] Y. Chyan, R. Ye, Y. Li, S.P. Singh, C.J. Arnusch, J.M. Tour, Laser-Induced Graphene by Multiple Lasing: Toward Electronics on Cloth, Paper, and Food, ACS Nano 12 (2018) 2176–2183. https://doi.org/10.1021/acsnano.7b08539.

[15] J. De La Roche, I. López-Cifuentes, A. Jaramillo-Botero, Influence of lasing parameters on the morphology and electrical resistance of polyimide-based laser-induced graphene (LIG), Carbon Lett. 33 (2023) 587–595. https://doi.org/10.1007/s42823-022-00447-2.

[16] H. Yuk, B. Lu, X. Zhao, Hydrogel bioelectronics, Chem. Soc. Rev. 48 (2019) 1642–1667. https://doi.org/10.1039/C8CS00595H.

[17] M.K. Yazdi, V. Vatanpour, A. Taghizadeh, M. Taghizadeh, M.R. Ganjali, M.T. Munir, S. Habibzadeh, M.R. Saeb, M. Ghaedi, Hydrogel membranes: A review, Materials Science and Engineering: C 114 (2020) 111023. https://doi.org/10.1016/j.msec.2020.111023.

[18] Y.S. Zhang, A. Khademhosseini, Advances in engineering hydrogels, Science 356 (2017) eaaf3627. https://doi.org/10.1126/science.aaf3627.

[19] G.J. Rodriguez-Rivera, A. Post, M. John, S. Buchan, D. Bernard, M. Razavi, E. Cosgriff-Hernandez, Injectable hydrogel electrodes as conduction highways to restore native pacing, Nat Commun 15 (2024) 64. https://doi.org/10.1038/s41467-023-44419-0.

[20] D. Seliktar, Designing Cell-Compatible Hydrogels for Biomedical Applications, Science 336 (2012) 1124–1128. https://doi.org/10.1126/science.1214804.

[21] K. Samoson, A. Soleh, K. Saisahas, K. Promsuwan, J. Saichanapan, P. Kanatharana, P. Thavarungkul, K.H. Chang, A.F. Lim Abdullah, K. Tayayuth, W. Limbut, Facile fabrication of a flexible laser induced gold nanoparticle/chitosan/ porous graphene electrode for uric acid detection, Talanta 243 (2022) 123319. https://doi.org/10.1016/j.talanta.2022.123319.

[22] H. Yoon, J. Nah, H. Kim, S. Ko, M. Sharifuzzaman, S.C. Barman, X. Xuan, J. Kim, J.Y. Park, A chemically modified laser-induced porous graphene based flexible and ultrasensitive electrochemical biosensor for sweat glucose detection, Sensors and Actuators B: Chemical 311 (2020) 127866. https://doi.org/10.1016/j.snb.2020.127866.

[23] Z. Zhao, R. Fang, Q. Rong, M. Liu, Bioinspired Nanocomposite Hydrogels with Highly Ordered Structures, Advanced Materials 29 (2017) 1703045. https://doi.org/10.1002/adma.201703045.

[24] The diffusion of electrolytes in a cation-exchange resin membrane I. Theoretical, Proc. R. Soc. Lond. A 232 (1955) 498–509. https://doi.org/10.1098/rspa.1955.0234.

[25] M.H. Cohen, D. Turnbull, Molecular Transport in Liquids and Glasses, The Journal of Chemical Physics 31 (1959) 1164–1169. https://doi.org/10.1063/1.1730566.

[26] R.I. Cukier, Diffusion of Brownian spheres in semidilute polymer solutions, Macromolecules 17 (1984) 252–255. https://doi.org/10.1021/ma00132a023.

[27] M. Kanduč, W.K. Kim, R. Roa, J. Dzubiella, How the Shape and Chemistry of Molecular Penetrants Control Responsive Hydrogel Permeability, ACS Nano 15 (2021) 614–624. https://doi.org/10.1021/acsnano.0c06319.

[28] Y. Ma, S.M. Morozova, E. Kumacheva, From Nature-Sourced Polysaccharide Particles to Advanced Functional Materials, Advanced Materials (2024) 2312707. https://doi.org/10.1002/adma.202312707.

[29] S. Smidstrup, T. Markussen, P. Vancraeyveld, J. Wellendorff, J. Schneider, T. Gunst, B. Verstichel, D. Stradi, P.A. Khomyakov, U.G. Vej-Hansen, M.-E. Lee, S.T. Chill, F. Rasmussen, G. Penazzi, F. Corsetti, A. Ojanperä, K. Jensen, M.L.N. Palsgaard, U. Martinez, A. Blom, M. Brandbyge, K. Stokbro, QuantumATK: an integrated platform of electronic and atomic-scale modelling tools, J. Phys.: Condens. Matter 32 (2020) 015901. https://doi.org/10.1088/1361-648X/ab4007.

[30] M.J. van Setten, M. Giantomassi, E. Bousquet, M.J. Verstraete, D.R. Hamann, X. Gonze, G.-M. Rignanese, The PseudoDojo: Training and grading a 85 element optimized norm-conserving pseudopotential table, Computer Physics Communications 226 (2018) 39–54. https://doi.org/10.1016/j.cpc.2018.01.012.

[31] J.M. Soler, E. Artacho, J.D. Gale, A. García, J. Junquera, P. Ordejón, D. Sánchez-Portal, The SIESTA method for *ab initio* order- *N* materials simulation, J. Phys.: Condens. Matter 14 (2002) 2745–2779. https://doi.org/10.1088/0953-8984/14/11/302.

[32] S.L. Mayo, B.D. Olafson, W.A. Goddard, DREIDING: a generic force field for molecular simulations, J. Phys. Chem. 94 (1990) 8897–8909. https://doi.org/10.1021/j100389a010.

[33] L. Martínez, R. Andrade, E.G. Birgin, J.M. Martínez, P ACKMOL : A package for building initial configurations for molecular dynamics simulations, J Comput Chem 30 (2009) 2157–2164. https://doi.org/10.1002/jcc.21224.

[34] K.-H. Nam, M. Abdulhafez, E. Castagnola, G.N. Tomaraei, X.T. Cui, M. Bedewy, Laser direct write of heteroatom-doped graphene on molecularly controlled polyimides for electrochemical biosensors with nanomolar sensitivity, Carbon 188 (2022) 209–219. https://doi.org/10.1016/j.carbon.2021.10.010.

[35] K.-H. Nam, M. Abdulhafez, G. Najaf Tomaraei, M. Bedewy, Laser-Induced fluorinated graphene for superhydrophobic surfaces with anisotropic wetting and switchable adhesion, Applied Surface Science 574 (2022) 151339. https://doi.org/10.1016/j.apsusc.2021.151339.

[36] M. Liu, J. Wu, H. Cheng, Effects of laser processing parameters on properties of laser-induced graphene by irradiating CO2 laser on polyimide, Sci. China Technol. Sci. 65 (2022) 41–52. https://doi.org/10.1007/s11431-021-1918-8.

[37] S. Deshmukh, P. Jakobczyk, M. Ficek, J. Ryl, D. Geng, R. Bogdanowicz, Tuning the Laser-Induced Processing of 3D Porous Graphenic Nanostructures by Boron-Doped Diamond Particles for Flexible Microsupercapacitors, Adv Funct Materials 32 (2022) 2206097. https://doi.org/10.1002/adfm.202206097.

[38] M. Jin, H.-K. Jeong, T.-H. Kim, K.P. So, Y. Cui, W.J. Yu, E.J. Ra, Y.H. Lee, Synthesis and systematic characterization of functionalized graphene sheets generated by thermal exfoliation at low temperature, J. Phys. D: Appl. Phys. 43 (2010) 275402. https://doi.org/10.1088/0022-3727/43/27/275402.

[39] D.W. Zeng, K.C. Yung, C.S. Xie, XPS investigation of the chemical characteristics of Kapton films ablated by a pulsed TEA CO2 laser, Surface and Coatings Technology 153 (2002) 210–216. https://doi.org/10.1016/S0257-8972(01)01696-6.

[40] M. Ayiania, M. Smith, A.J.R. Hensley, L. Scudiero, J.-S. McEwen, M. Garcia-Perez, Deconvoluting the XPS spectra for nitrogen-doped chars: An analysis from first principles, Carbon 162 (2020) 528–544. https://doi.org/10.1016/j.carbon.2020.02.065.

[41] A.C. Ferrari, Raman spectroscopy of graphene and graphite: Disorder, electron–phonon coupling, doping and nonadiabatic effects, Solid State Communications 143 (2007) 47–57. https://doi.org/10.1016/j.ssc.2007.03.052.

[42] M.A. Pimenta, G. Dresselhaus, M.S. Dresselhaus, L.G. Cançado, A. Jorio, R. Saito, Studying disorder in graphite-based systems by Raman spectroscopy, Phys. Chem. Chem. Phys. 9 (2007) 1276–1290. https://doi.org/10.1039/B613962K.

[43] V. Thapliyal, M.E. Alabdulkarim, D.R. Whelan, B. Mainali, J.L. Maxwell, A concise review of the Raman spectra of carbon allotropes, Diamond and Related Materials 127 (2022) 109180. https://doi.org/10.1016/j.diamond.2022.109180.

[44] X.D. Huang, S.M. Bhangale, P.M. Moran, N.L. Yakovlev, J. Pan, Surface modification studies of Kapton ® HN polyimide films, Polymer International 52 (2003) 1064–1069. https://doi.org/10.1002/pi.1143.

[45] M.D. Hossain, Q. Zhang, T. Cheng, W.A. Goddard, Z. Luo, Graphitization of low-density amorphous carbon for electrocatalysis electrodes from ReaxFF reactive dynamics, Carbon 183 (2021) 940–947. https://doi.org/10.1016/j.carbon.2021.07.080.

[46] S. Jeong, Y. Ito, Y. Kwon, H. Sun, J. Chung, M. Suk, N. Sugita, Unveiling the Potential of Colorless Polyimide-Derived Laser-Induced Graphene: A Novel Pathway for Advanced Sensor and Energy Harvester Performance, Adv Materials Inter 10 (2023) 2300625. https://doi.org/10.1002/admi.202300625.

[47] A. Ghavipanjeh, S. Sadeghzadeh, Simulation and experimental evaluation of laser-induced graphene on the cellulose and lignin substrates, Sci Rep 14 (2024) 4475. https://doi.org/10.1038/s41598-024-54982-1.

[48] D. Martín-Yerga, E. Costa Rama, A. Costa García, Electrochemical Study and Determination of Electroactive Species with Screen-Printed Electrodes, J. Chem. Educ. 93 (2016) 1270–1276. https://doi.org/10.1021/acs.jchemed.5b00755.

[49] M. Cieślik, A. Susik, M. Banasiak, R. Bogdanowicz, K. Formela, J. Ryl, Tailoring Diamondised Nanocarbon-Loaded Poly(lactic acid) Composites for Highly Electroactive Surfaces: Extrusion and Characterisation of filaments for Improved 3D printed Surfaces, Microchimica Acta accepted (2023).

[50] K. Avinash, F. Patolsky, Laser-induced graphene structures: From synthesis and applications to future prospects, Materials Today 70 (2023) 104–136. https://doi.org/10.1016/j.mattod.2023.10.009.

[51] M.T. Rauter, S.K. Schnell, S. Kjelstrup, Cassie–Baxter and Wenzel States and the Effect of Interfaces on Transport Properties across Membranes, J. Phys. Chem. B 125 (2021) 12730–12740. https://doi.org/10.1021/acs.jpcb.1c07931.

[52] A.J. Bard, L.R. Faulkner, H.S. White, Electrochemical methods: fundamentals and applications, Third edition, Wiley, Hoboken, NJ, 2022.

[53] A.V. Shokurov, C. Menon, Laser-Induced Graphene Electrodes for Electrochemistry Education and Research, J. Chem. Educ. 100 (2023) 2411–2417. https://doi.org/10.1021/acs.jchemed.2c01237.

[54] D. Wang, Z. Zhang, J. Zhang, X. Deng, Z. Fan, G. Tang, Electronic and magnetic properties of zigzag-edged hexagonal graphene ring nanojunctions, Carbon 94 (2015) 996–1002. https://doi.org/10.1016/j.carbon.2015.07.082.

[55] A. Olejnik, M. Ficek, M. Szkodo, A. Stanisławska, J. Karczewski, J. Ryl, A. Dołęga, K. Siuzdak, R. Bogdanowicz, Tailoring Diffusional Fields in Zwitterion/Dopamine Copolymer Electropolymerized at Carbon Nanowalls for Sensitive Recognition of Neurotransmitters, ACS Nano 16 (2022) 13183–13198. https://doi.org/10.1021/acsnano.2c06406.

[56] J. Moldenhauer, M. Meier, D.W. Paul, Rapid and Direct Determination of Diffusion Coefficients Using Microelectrode Arrays, J. Electrochem. Soc. 163 (2016) H672–H678. https://doi.org/10.1149/2.0561608jes.

[57] Y. Wang, J.G. Limon-Petersen, R.G. Compton, Measurement of the diffusion coefficients of [Ru(NH3)6]3+ and [Ru(NH3)6]2+ in aqueous solution using microelectrode double potential step chronoamperometry, Journal of Electroanalytical Chemistry 652 (2011) 13–17. https://doi.org/10.1016/j.jelechem.2010.12.011.

[58] P. Xiong, L. Zhang, Y. Chen, S. Peng, G. Yu, A Chemistry and Microstructure Perspective on Ion-Conducting Membranes for Redox Flow Batteries, Angew Chem Int Ed 60 (2021) 24770–24798. https://doi.org/10.1002/anie.202105619.

[59] F. Yu, A.C. Stoot, P. Bøggild, L. Camilli, Failure of multi-layer graphene coatings in acidic media, RSC Adv. 6 (2016) 21497–21502. https://doi.org/10.1039/C6RA01556E.

[60] D.S. Chauhan, V. Srivastava, P.G. Joshi, M.A. Quraishi, PEG cross-linked Chitosan: a biomacromolecule as corrosion inhibitor for sugar industry, Int J Ind Chem 9 (2018) 363–377. https://doi.org/10.1007/s40090-018-0165-0.

[61] M. Khnifira, W. Boumya, J. Attarki, A. Mahsoune, M. Abdennouri, M. Sadiq, S. Kaya, N. Barka, Elucidating the adsorption mechanisms of anionic dyes on chitosan (110) surface in aqueous medium by quantum chemical and molecular dynamics, Materials Today Communications 33 (2022) 104488. https://doi.org/10.1016/j.mtcomm.2022.104488.